



Rapid electron transfer via hetero-interface engineering of 2D MOF anchored Ti_3C_2 MXene nanosheet for enhanced photocatalytic disinfection

Jianfang Li^a, Zhenxing Yang^b, Chaofeng Wang^c, Shuilin Wu^{d,*}, Yufeng Zheng^d, Zhenduo Cui^e, Hui Jiang^e, Zhaoyang Li^e, Shengli Zhu^e, Liheng Feng^{a,*}, Xiangmei Liu^{b,c, **}

^a School of Chemistry and Chemical Engineering, Shanxi University, Taiyuan 030006, China

^b Biomedical Materials Engineering Research Center, Hubei Key Laboratory of Polymer Materials, Ministry-of-Education Key Laboratory for the Green Preparation and Application of Functional Materials, School of Materials Science and Engineering, Hubei University, Wuhan 430062, China

^c School of Health Science & Biomedical Engineering, Hebei University of Technology, Xiping Avenue 5340, Beichen District, Tianjin 300401, China

^d School of Materials Science & Engineering, Peking University, Yiheyuan Road 5#, Beijing 100871, China

^e School of Materials Science & Engineering, The Key Laboratory of Advanced Ceramics and Machining Technology by the Ministry of Education of China, Tianjin University, Tianjin 300072, China



ARTICLE INFO

Keywords:

Hetero-interface engineering
Photocatalysis

2D MOF

Ti_3C_2 MXene

Disinfection

ABSTRACT

Photocatalytic materials are one of the most promising alternatives of antibiotics for wound disinfection, and the bacteria-killing efficacy is restrained by photocatalytic performance. Herein, Ti_3C_2 MXene-anchored 2D metal-organic frame (MOF) nanosheets were constructed to enhance the photocatalytic performance through interface engineering strategy by in-situ growth of 2D MOF on Ti_3C_2 nanosheets. On the one hand, the close contact between them decreased the bandgap of 2D MOF, improving the yield of photogenerated electrons. On the other hand, it not only provided a rapid electron transfer channel across the interface but also induced the formation of Schottky junction at the interface. Consequently, the separation efficiency of photo-generated electron-hole pairs was significantly enhanced by rapid transfer and inhibition of electron backflow. Thus, under 660 nm plus 808 nm light, MOF/ Ti_3C_2 killed $99.73 \pm 0.12\%$ of *Staphylococcus aureus*. This work will provide insights for designing photo-responsive materials through in-situ interfacial engineering strategies.

1. Introduction

Bacterial infections are one of the leading causes of human deaths around the world. The mainstreaming of the clinic is the use of antibiotics. However, the overuse of antibiotics increases bacterial resistance, even the emergence of super-bacteria [1–3]. The latest reports disclosed that 4.95 million people died from illnesses associated with bacterial resistance in 2019 [4]. Therefore, the development of non-antibiotic antibacterial techniques is key to reducing the misuse of antibiotics. The reactive oxygen species (ROS) generated by photosensitizers can effectively kill bacteria that do not create resistance. The increased yield of ROS is crucial, which can make efforts from light absorption, the generation of carriers, efficient charge separation and transfer, and redox reaction on the surface [5,6].

Two-dimensional (2D) materials with ultrathin thickness are

beneficial for light absorption [7]. The different chemical structures and crystal symmetries can provide tunable photoelectric properties. And the low exciton binding energy of 2D materials can decrease the recombination of electrons and holes [8]. Recently, many 2D photocatalysts are used for photodynamic therapy, such as C_3N_4 , black phosphorus, transition metal dichalcogenides, and so on [9,10]. Compared with these 2D materials, metal-organic frameworks (MOFs) are porous coordination polymer materials constructed by metal nodes and organic ligands [11], which have attracted great attention in gas sorption, catalysis, and energy storage and conversion [12]. 2D porphyrin-based MOFs nanosheets with good stability exhibit photo-responsive characteristics due to the light absorption ability and photonic functionality of porphyrins [13]. Based on porphyrin complexation with copper, Cu(II) tetra(4-carboxyphenyl)porphyrin (Cu-TCPP) nanosheets have good protonic conductivity, porous

* Corresponding authors.

** Corresponding author at: Biomedical Materials Engineering Research Center, Hubei Key Laboratory of Polymer Materials, Ministry-of-Education Key Laboratory for the Green Preparation and Application of Functional Materials, School of Materials Science and Engineering, Hubei University, Wuhan 430062, China.

E-mail addresses: slwu@pku.edu.cn (S. Wu), lhfeng@sxu.edu.cn (L. Feng), liuxiangmei1978@163.com (X. Liu).

structure, and good stability [14]. However, its low electrical conductivity reduces the utilization of photogenerated carriers. And the recombination of electrons and holes reduced the yield of ROS.

Compared to single 2D materials, 2D heterojunction have high specific surface area, large active sites, and facile charge transport path [15, 16]. The intact contact of 2D materials can provide efficient electron transfer channel to separate photogenerated electron-hole pairs [17]. Thus, 2D heterojunction interface engineering becomes an effective strategy to improve the utilization of electrons and holes. 2D Ti_3C_2 MXene nanosheets have excellent conductivity, which can improve the transfer of electrons to inhibit the combination of photocarriers [18]. Besides, the biocompatible Ti_3C_2 nanosheets exhibit remarkable absorption under near-infrared regions [19]. The structure of Ti_3C_2 MXene-anchored 2D MOF may be beneficial to improve charge transfer and the utilization of photogenerated electrons, further producing more ROS and achieving efficient antibacterial activity [20,21].

In this work, we assumed if 2D MOF/ Ti_3C_2 MXene can form Schottky junction to improve the utilization of electrons and holes, reaching an excellent antibacterial effect under 660 nm plus 808 nm light. The intimate interface of 2D MOF and Ti_3C_2 with a relatively large surface area provided the charge transfer channel and accelerated the separation of electrons and holes, and the Schottky effect inhibited the backflow of electrons. Besides, the photothermal performance also improved the transfer of electrons. Under the synergy role, more ROS can be produced to kill $99.73 \pm 0.12\%$ against *Staphylococcus aureus* (*S. aureus*) under dual-light irradiation with the assistance of heat. This structural design for the development of novel MXenes heterojunctions and their applications in antibacterial performance provide sights.

2. Experimental

2.1. Materials

Ti_3AlC_2 was purchased from 11 technology Co., Ltd (Jilin, China). LiF, trifluoroacetic acid, N, N-dimethylformamide, and meso-tetra(4-carboxyphenyl) porphine were purchased from Aladdin Biochemical Technology Co., Ltd (Shanghai, China). Polyvinyl pyrrolidone was purchased from Yifang Technology Co., Ltd. Hydrochloric acid (HCl, 36.0 – 38.0%) was purchased from Jiangtian Chemical Technology Co., Ltd. Cupric acetate monohydrate ($\text{Cu}(\text{CH}_3\text{COO})_2 \cdot \text{H}_2\text{O}$) was purchased from Heowns Technology Co., Ltd.

2.2. Preparation of Ti_3C_2 MXene nanosheets

The preparation of 2D Ti_3C_2 nanosheets was fabricated by LiF/HCl method [22]. Briefly, 1 g of LiF and 10 mL of HCl were stirred for 15 min. 1 g of Ti_3AlC_2 was slowly added to the above and stirred at 40 °C for 24 h. The mixture was washed with deionized water until the pH of the supernatant was close to 6. The precipitate was redispersed and sonicated in an ice bath for 30 min. Subsequently, the mixture was centrifuged at 3500 rpm for 15 min to obtain a few layers of Ti_3C_2 MXene nanosheets. The Ti_3C_2 nanosheets were obtained by the freeze-drying method.

2.3. Preparation of Cu-TCPP/ Ti_3C_2 and Cu-TCPP

1, 3, 5, 7, and 10 mg Ti_3C_2 nanosheets were respectively dispersed into the solution of N, N-dimethylformamide (DMF) and ethanol with a volume ratio of 3:1. 0.0375 mmol of $\text{Cu}(\text{CH}_3\text{COO})_2 \cdot \text{H}_2\text{O}$, 25 μL of trifluoroacetic acid, and 25 mg of polyvinylpyrrolidone (PVP) were added and stirred for 30 min. 10 mg of meso-tetra(4-carboxyphenyl) porphine dissolved in a volume ratio of 3:1 of DMF and ethanol slowly dropped into the above solution. The mixture was heated at 80 °C for 3 h, and then washed with deionized water and dried under vacuum to obtain Cu-TCPP/ Ti_3C_2 , which was labeled as Cu-TCPP/ Ti_3C_2 -1, Cu-TCPP/ Ti_3C_2 -3, Cu-TCPP/ Ti_3C_2 -5, Cu-TCPP/ Ti_3C_2 -7, and Cu-TCPP/ Ti_3C_2 -10. The mass

ratios of Ti_3C_2 and Cu-TCPP determined by inductively coupled plasma optical emission spectrometry (ICP-OES, ICAP7000 series) were 1.89%, 4.98%, 8.46%, and 9.39%, respectively. Cu-TCPP was fabricated by the same methods without the addition of Ti_3C_2 .

2.4. Material morphology and structural characterization

The crystal structure of Ti_3C_2 , Cu-TCPP, and Cu-TCPP/ Ti_3C_2 was characterized using X-ray diffraction (XRD). The morphology was observed by field emission scanning electron microscopy (FESEM, S4800) and transmission electron microscopy (TEM, JEM 2100 F). The functional group was analyzed by Fourier transform infrared spectroscopy (FTIR, Thermo Scientific). The elemental composition was conducted using X-ray photoelectron spectroscopy (XPS, Axis Supra). The thickness was measured by atomic force microscope (AFM, Agilent 5500). UV-Vis absorbance spectra were performed by UV-Vis spectrophotometer (UV-2700). The zeta potential was measured by dynamic light scattering analysis (90 Plus/BIMAS). The photoluminescence (PL) curves were detected by fluorescence spectrophotometer (Fluorolog-3).

2.5. Photothermal property

200 μL of 300 ppm Ti_3C_2 , Cu-TCPP, and Cu-TCPP/ Ti_3C_2 suspension were irradiated under 808 (0.35 W cm^{-2}) + 660 nm (0.95 W cm^{-2}). The two light sources emitting 660 nm and 808 nm light were used. The temperature variation was recorded by a thermal imager.

2.6. Photocatalytic performance

Electrochemical property: The electrochemical property of Ti_3C_2 , Cu-TCPP, and Cu-TCPP/ Ti_3C_2 was performed in 0.5 mol L^{-1} Na_2SO_4 solution by electrochemical workstation (CHI660E). The standard three-electrode system was used to measure photocurrent and electrochemical impedance spectra (EIS). The Ag/AgCl electrode was used as the reference electrode, the Pt was used as the counter electrode, and the sample was used as the working electrode. The working electrode was prepared as follows: 4 mg of different materials were dispersed to the mixture of deionized water and ethanol and sonicated for 5 min. The uniform suspension was dropped on the FTO glass electrode and dried in the air.

The measurement of ROS: 2',7'-Dichlorodihydrofluorescein diacetate (DCFH-DA) was used to measure the production of ROS. DCFH-DA was hydrolyzed by phosphate buffer solution (PBS) to generate dichlorodihydrofluorescein (DCFH). DCFH can be oxidized by ROS generated by materials to produce fluorescent DCF. The fluorescence was measured by a microplate reader with an excitation of 488 nm and an emission of 525 nm. The yield of ROS was tested every 2 min. The yield of ROS of Ti_3C_2 , Cu-TCPP, and Cu-TCPP/ Ti_3C_2 was measured under 660 + 808 nm. The yield of ROS of Cu-TCPP/ Ti_3C_2 was also tested under 25 °C and 55 °C, respectively. The singlet oxygen (${}^1\text{O}_2$) produced by Cu-TCPP, and Cu-TCPP/ Ti_3C_2 was tested using electron paramagnetic resonance (EPR, JES-FA200, JEOL) spectrometer. And 2, 2, 6, 6-tetramethylpiperidine (TEMP) was used as a trapping agent. The ${}^1\text{O}_2$ was also measured by 1, 3-diphenylisobenzofuran (DPBF). Ti_3C_2 , Cu-TCPP, and Cu-TCPP/ Ti_3C_2 mixed with DPBF were placed under 660 + 808 nm light illumination. The variation of absorbance at 415 nm was measured by a microplate reader to verify the production of ${}^1\text{O}_2$. The generation of $\cdot\text{O}_2^-$ under light irradiation was tested by its characteristic reaction with the nitro blue tetrazolium (NBT). The absorbance was measured at 530 nm. The production of $\cdot\text{OH}$ was tested by aminophenylfluorescein (APF), which can be detected by measuring the fluorescence of oxidized APF. The fluorescence was measured at an excitation of 490 nm and an emission of 514 nm.

2.7. DFT calculation

The first-principle density functional theory (DFT) calculations were

performed by Vienna Ab initio Simulation Package (VASP) with the projector augmented wave (PAW) method. The exchange-functional was treated using the generalized gradient approximation (GGA) of Perdew-Burke-Ernzerhof (PBE) functional. The energy cutoff for the plane wave basis expansion was set to 450 eV and the force on each atom less than 0.03 eV/Å was set for the convergence criterion of geometry relaxation. The self-consistent calculations apply a convergence energy threshold of 10^{-5} eV.

2.8. Ion release

Cu-TCPP and Cu-TCPP/Ti₃C₂ were soaked in 100 mL of deionized water with the final concentration of 300 ppm. 3 mL of the supernatant was taken out at 20 min, 2, 6, 12 h, 1, 2, 4, 6, 10, 12 d, respectively. And add another 3 mL of fresh deionized water. The concentration of Cu ions was measured by ICP-OES. To assess the photo-stability of Cu-TCPP/Ti₃C₂, 200 μ L suspension containing Cu-TCPP/Ti₃C₂ with a concentration of 300 ppm was irradiated under 660 + 808 nm for 20 min. After that, the materials were centrifuged and the concentration of Cu ions was measured by ICP-OES.

2.9. Antibacterial property

Staphylococcus aureus (*S. aureus*, 10^7 CFU mL⁻¹) was used as the experimental strain.

Spread plate method: 200 μ L bacterial suspension containing Cu-TCPP/Ti₃C₂-1, Cu-TCPP/Ti₃C₂-3, Cu-TCPP/Ti₃C₂-5, and Cu-TCPP/Ti₃C₂-7 with a final concentration of 300 ppm was measured under 660 nm (0.95 W cm⁻²) + 808 (0.35 W cm⁻²) light for 20 min. The diluted bacterial suspension was incubated on the plate at 37 °C for 20 h. The bacterial colony number was photographed and counted.

200 μ L of bacterial suspension containing Ti₃C₂, Cu-TCPP, and Cu-TCPP/Ti₃C₂ with a final concentration of 300 ppm was measured under 660 nm (0.95 W cm⁻²) + 808 (0.35 W cm⁻²) light or dark for 20 min under static conditions, respectively. The diluted bacterial suspension was incubated on the plate at 37 °C for 20 h. The number of bacterial colonies was photographed and counted. The antibacterial performance of Cu-TCPP/Ti₃C₂ was also measured by the same method under 660 nm (0.95 W cm⁻²) or 808 (0.35 W cm⁻²) light alone.

To measure the long-term antibacterial property, the same concentrations of Ti₃C₂, Cu-TCPP, and Cu-TCPP/Ti₃C₂ were mixed with the bacterial suspension. Subsequently, the bacterial suspension was incubated on a shaker at 150 rpm for 2 and 6 h, respectively. The diluted bacterial suspension was incubated on the plate for 20 h to count the antibacterial rate.

To evaluate the influence of ROS alone on the antibacterial effect of Cu-TCPP/Ti₃C₂, the experiment was tested in an ice-water bath. The antibacterial performance was measured by the spread plate method. For the role of heat for antibacterial performance, the bacterial suspension containing Cu-TCPP/Ti₃C₂ was placed in a water bath. The temperature was increased according to the temperature curve under 660 + 808 nm. In the cycling experiments of bacterial performance, the bacterial suspension containing Cu-TCPP/Ti₃C₂ was irradiated again after the end of the antibacterial test.

SEM of bacteria: Ti₃C₂, Cu-TCPP, and Cu-TCPP/Ti₃C₂ suspension mixed with *S. aureus* were placed in a 96-well plate, which was treated under static conditions with 660 + 808 nm or dark for 20 min. The bacteria were fixed with 4% glutaraldehyde for 40 min, followed by dehydration using graded ethanol (10%, 30%, 50%, 70%, 90%, and 100%). The morphologies of bacteria were observed by SEM.

Live-dead staining of bacteria: The treated bacteria with Ti₃C₂, Cu-TCPP, and Cu-TCPP/Ti₃C₂ under 660 + 808 nm or in the dark for 20 min were stained using SYTO9 and PI for 20 min and then rinsed with PBS for three times. The bacteria were observed by inverted fluorescence microscopy. The fluorescence of SYTO9 and PI was measured at an excitation of 488, 561 nm, respectively.

The permeability of bacterial membrane: O-nitrophenyl- β -D-galactopyranoside (ONPG) was used to measure the permeability. The bacteria were cultured in Luria-Bertani (LB) medium with isopropyl β -D-1-thiogalactopyranoside. After 12 h, the bacteria were washed with PBS and dispersed to PBS. After being treated with different materials with or without light, the absorbance of the supernatant was measured at 420 nm.

The integrity of bacterial membrane: The bacterial suspension containing Ti₃C₂, Cu-TCPP, and Cu-TCPP/Ti₃C₂ was treated under 660 + 808 nm or dark for 20 min. The absorbance of the supernatant at 260 nm was measured.

2.10. Biocompatibility *in vitro*

Cell cytotoxicity was assessed via 3-(4, 5-dimethylthiazol-2-yl)-2, 5-diphenyltetrazolium bromide (MTT) assay. 200 μ L of L929 cell suspension was incubated on a 96-well plate for 24 h. 300 ppm Ti₃C₂, Cu-TCPP, and Cu-TCPP/Ti₃C₂ were dipped in the cell culture medium for 3 d. The leach liquors were used to incubate cells. After reaching the indicated time, the cytotoxicity of materials was tested by the absorbance at 490 nm.

Cell fluorescence: L929 cells were cultured in 96 wells. After 24 h, the cells were cultured with the leach liquors. At the appointed time, the cells were fixed with 4% formaldehyde. After 30 min, these cells were stained with 4',6-diamidino-2-phenylindole (DAPI) and FITC-conjugated phalloidin. The cell was observed by laser scanning confocal microscope. The fluorescence of DAPI and FITC was detected using 405 and 488 nm laser excitation wavelengths.

2.11. Animal wound model

The animals used in this experiment were male Wistar rats (approximately 300 g). The animal experiment was approved by the Institutional Animal Care and Use Committee of Yi Shengyuan Gene Technology (Tianjin) Co., Ltd. The rats were randomly divided into Ctrl, Cu-TCPP/Ti₃C₂ + light (-), and Cu-TCPP/Ti₃C₂ + light (+) groups. After 3 days, these rats were anesthetized and a wound with a diameter of 16 mm was cut on their backs. 50 μ L of *S. aureus* (10^7 CFU mL⁻¹) was dropped to the wound and waited for 20 min. The wound of Ctrl group was injected with 50 μ L of PBS. The wound of Cu-TCPP/Ti₃C₂ + light (-) and Cu-TCPP/Ti₃C₂ + light (+) groups were injected with 50 μ L of Cu-TCPP/Ti₃C₂ suspension (600 ppm). The wound of the Ctrl and Cu-TCPP/Ti₃C₂ + light (-) groups were placed for 20 min. The Cu-TCPP/Ti₃C₂ + light (+) group was irradiated under 660 + 808 nm for 20 min. All wounds were wrapped in gauze. The wounds were photographed at 2, 7, and 12 d to observe the healing of the wounds. In addition, tissues around the wounds were taken for hematoxylin-eosin (H&E) staining, Giemsa staining, and Masson staining at 2 and 12 d, respectively. H&E staining of the heart, liver, spleen, lung, and kidney was performed on 12 d.

2.12. Statistical Analysis

All the quantitative data in each experiment were presented and analyzed by one-way or two-way analysis of variance and expressed as the mean values \pm standard deviations, followed by Tukey's multiple comparisons post hoc test to evaluate the statistical significance of the variance. The *n. s.* present $P > 0.05$ and * ** * $P < 0.0001$ were considered statistically significant.

3. Results and discussion

3.1. Characterization of Ti₃C₂, Cu-TCPP, and Cu-TCPP/Ti₃C₂

To fabricate Cu-TCPP/Ti₃C₂, Ti₃AlC₂ firstly was etched by LiF/HCl methods. As depicted in Fig. 1a, Ti₃AlC₂ was exfoliated to monolayer or

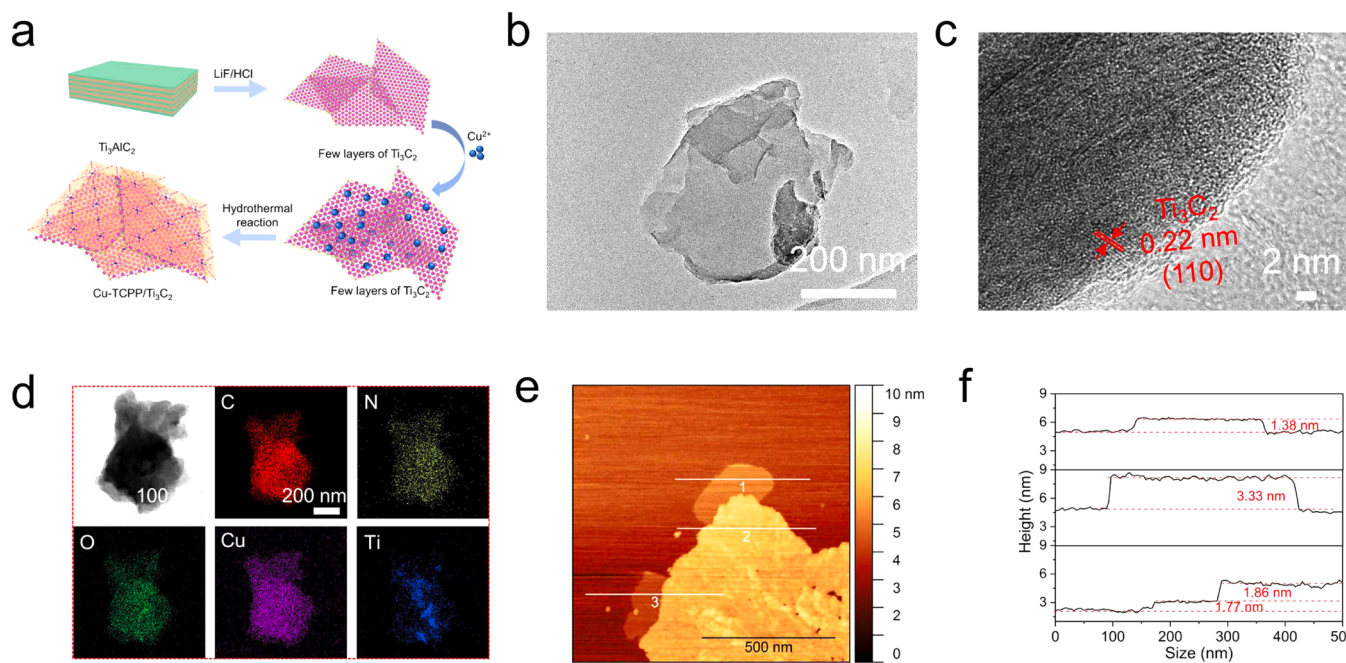


Fig. 1. Schematic illustration and morphology of Cu-TCPP/Ti₃C₂ heterostructure. (a) Schematic illustration for constructing the Cu-TCPP/Ti₃C₂ heterostructure. (b-c) TEM and HRTEM images of Cu-TCPP/Ti₃C₂. (d) The mapping of C, N, Cu, O, and Ti elements for Cu-TCPP/Ti₃C₂. (e) AFM image of Cu-TCPP/Ti₃C₂. (f) The height profiles of Cu-TCPP/Ti₃C₂.

few layers of Ti_3C_2 after etching. During this process, the surface of Ti_3C_2 was endowed with abundant functional groups, including -OH, -O, which resulted in the negatively charged surface. Thus, Cu^{2+} can be adsorbed to the surface of Ti_3C_2 . Through the simple solvothermal process, Cu-TCPP was anchored to Ti_3C_2 MXene nanosheets to obtain Cu-TCPP/Ti₃C₂. Firstly, the morphology was observed by scanning electron microscopy (SEM). As shown in Fig. S1a, Ti_3C_2 exhibited ultrathin nanosheet morphology with a smooth surface. Cu-TCPP showed

the 2D nanosheet-like structure (Fig. S1b). After the combination of Cu-TCPP and Ti_3C_2 , the sheet-like structure can be observed for Cu-TCPP/Ti₃C₂-1, Cu-TCPP/Ti₃C₂-3, Cu-TCPP/Ti₃C₂-5, and Cu-TCPP/Ti₃C₂-7 (Fig. S1c-f). No obvious nanosheet structure can be observed for Cu-TCPP/Ti₃C₂-10 (Fig. S1g). The transmission electron microscopy (TEM) images of Ti_3C_2 revealed the almost transparent nanosheets (Fig. S2a). The high-resolution TEM (HRTEM) image of Ti_3C_2 nanosheets showed a lattice spacing of 0.22 nm, which is assignable to Ti_3C_2 (110) planes

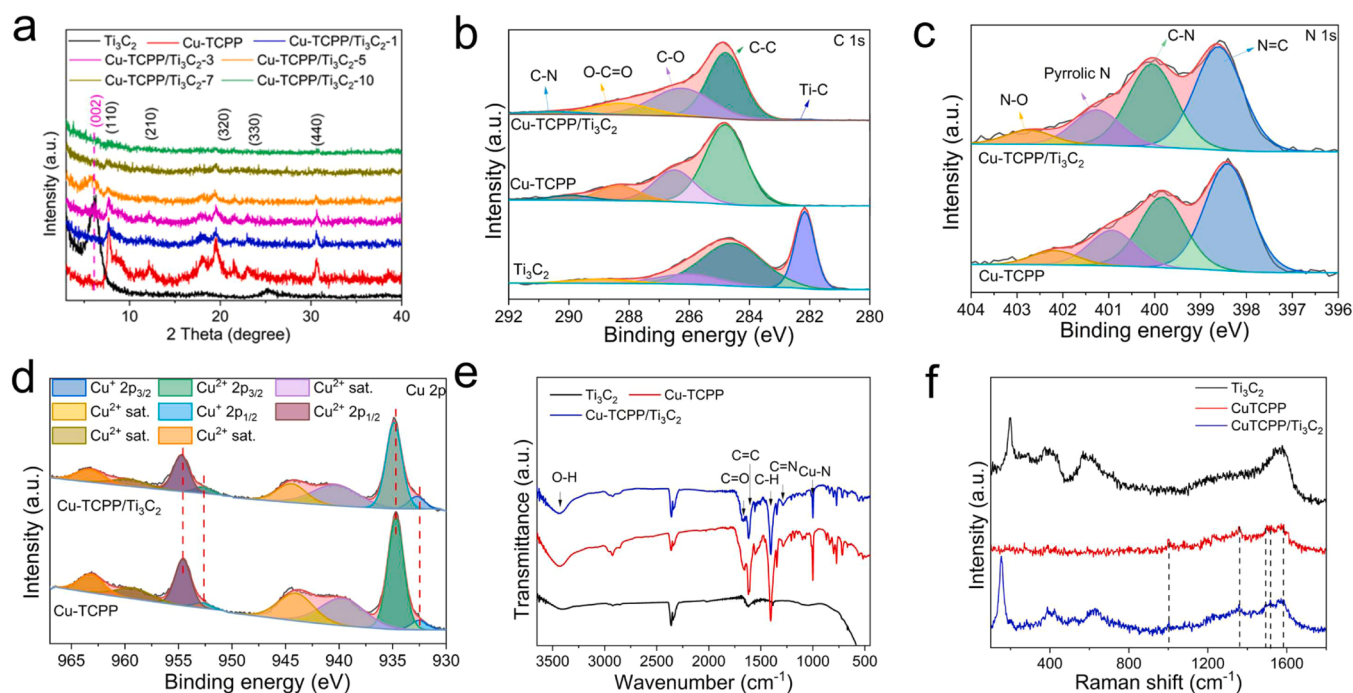


Fig. 2. Characterization of Ti_3C_2 , Cu-TCPP, and Cu-TCPP/Ti₃C₂. (a) XRD patterns. (b) High-resolution spectra of C 1s of Ti_3C_2 , Cu-TCPP, and Cu-TCPP/Ti₃C₂. (c) High-resolution spectra of N 1s for Cu-TCPP and Cu-TCPP/Ti₃C₂. (d) High-resolution spectra of Cu 2p for Cu-TCPP and Cu-TCPP/Ti₃C₂. (e) FTIR spectra. (f) Raman spectra.

(Fig. S2b) [23]. The TEM image of Cu-TCPP displayed a typical nanosheet structure (Fig. S2c). As a consequence of the weak diffraction of Cu-TCPP, no obvious lattice can be observed (Fig. S2d) [24]. Cu-TCPP/Ti₃C₂ revealed the structure of nanosheets overlapping each other in Fig. 1b. HRTEM image (Fig. 1c) contained an interplanar spacing of 0.22 nm and non-lattice structures, corresponding to (110) crystal plane of Ti₃C₂ and Cu-TCPP. The elements mapping in Fig. 1d can observe the distribution of C, N, Cu, O, and Ti elements of Cu-TCPP/Ti₃C₂, indicating the successful recombination of Cu-TCPP and Ti₃C₂. Such an intimate interface between Cu-TCPP and Ti₃C₂ facilitated the separation and migration of photocarriers. The atomic force microscopy (AFM) of Ti₃C₂, Cu-TCPP, and Cu-TCPP/Ti₃C₂ was exhibited in Fig. S3 and Fig. 1e. The thickness of nanosheet for Ti₃C₂ and Cu-TCPP was about 2.35, 4.07 nm, respectively. Cu-TCPP/Ti₃C₂ exhibited nanosheet structure and atomically flat surface morphology. The line profile in Fig. 1f displayed the thickness was about 3.48 nm.

X-ray diffraction (XRD) patterns in Fig. 2a exhibited a strong diffraction peak for Ti₃C₂ at 6.25°, corresponding to the (002) plane. No obvious impurity peak can be observed, indicating the successful fabrication of Ti₃C₂ nanosheets. XRD of Cu-TCPP showed (110), (210), (320), (330), and (440) lattice plane, which was consistence with the previous paper [25]. After the combination of Ti₃C₂ and Cu-TCPP, XRD patterns of Cu-TCPP/Ti₃C₂-X contained the characteristic peaks of Cu-TCPP and Ti₃C₂ nanosheets. As the increase of Ti₃C₂ content, the peaks of Cu-TCPP gradually weaken, even vanishing for Cu-TCPP/Ti₃C₂-10. Thus, the excess Ti₃C₂ nanosheets can affect the formation of Cu-TCPP, which might result from the excess Ti participating in the metal node position of Cu-TCPP.

The survey spectra of Cu-TCPP/Ti₃C₂ of X-ray photoelectron spectroscopy (XPS) in Fig. S4 observed the signal peaks of Cu 2p, Ti 2p, O 1 s, N 1 s, and C 1 s, while Ti₃C₂ only had Ti 2p, O 1 s, and C 1 s peaks and Cu-TCPP had Cu 2p, O 1 s, N 1 s, and C 1 s peaks. The high-resolution spectra of C 1 s of Cu-TCPP in Fig. 2b belong to C-N, O-C=C, C-O, and C-C peaks [26]. C 1 s spectrum of Ti₃C₂ appeared Ti-C, O-C=C, C-O, and C-C peaks [27]. Cu-TCPP/Ti₃C₂ exhibited five peaks, belonging to C-N, O-C=C, C-O, Ti-C, and C-C bonds. The high-resolution spectra of N 1 s in Fig. 2c can be divided into four peaks, including N-O, pyrrolic N, C-N, and N=C for Cu-TCPP and Cu-TCPP/Ti₃C₂. Also, Cu 2p spectrum of Cu-TCPP and Cu-TCPP/Ti₃C₂ nanosheets revealed the signals of the Cu²⁺ 2p_{1/2}, Cu⁺ 2p_{1/2}, Cu²⁺ 2p_{3/2}, and Cu⁺ 2p_{3/2} (Fig. 2d) [28]. Compared to Cu-TCPP, the peaks of Cu 2p of Cu-TCPP/Ti₃C₂ slightly shifted to the higher binding energy, suggesting the strong interaction of Cu-TCPP and Ti₃C₂.

The Fourier transform infrared spectrometer (FTIR) spectra in Fig. 2e revealed that the peak near 1670 and 1620 cm⁻¹ was assigned to C=O and C=C stretching vibrations. The peaks at 1400 cm⁻¹ corresponded to C-H stretching vibrations. The peak around 1290 cm⁻¹ was ascribed to C=N stretching vibrations. The peak of N-Cu stretching vibrations was close to 1000 cm⁻¹ [29]. The broad band at 3000–3500 cm⁻¹ originated from hydroxyl groups. Raman spectra in Fig. 2f of Cu-TCPP/Ti₃C₂ exhibited distinct characteristic bands of Cu-TCPP and Ti₃C₂. Especially, 148, 383, and 624 cm⁻¹ originated from Ti₃C₂ MXene [30].

Additionally, zeta potential in Fig. S5 was used to verify the process of preparation. Zeta potential of Ti₃C₂ nanosheets was -24.95 ± 2.82 mV. Thus, Ti₃C₂ nanosheets can adsorb Cu²⁺ by electrostatic interaction. Zeta potential of pristine Cu-TCPP and Cu-TCPP/Ti₃C₂ were -10.54 ± 0.96 , -20.71 ± 1.09 mV, respectively.

3.2. The photocatalytic and photothermal performance of Cu-TCPP/Ti₃C₂

Electron transfer is a very critical factor for photocatalytic performance. Thus, the photocurrent density of Cu-TCPP, Cu-TCPP/Ti₃C₂-1, Cu-TCPP/Ti₃C₂-3, Cu-TCPP/Ti₃C₂-5, and Cu-TCPP/Ti₃C₂-7 was measured under 660 + 808 nm in Fig. S6. Compared to Cu-TCPP, all of Cu-TCPP/Ti₃C₂-X improved photocurrent densities, indicating the

enhanced the ability of charge separation. Cu-TCPP/Ti₃C₂-5 exhibited the largest photocurrent density, demonstrating the best transfer and separation of photo-generated electrons at this ratio between Cu-TCPP and Ti₃C₂. Thus, the Cu-TCPP/Ti₃C₂-5 was used as the ultimate content.

Fig. 3a exhibited the light absorption of Ti₃C₂, Cu-TCPP, and Cu-TCPP/Ti₃C₂ from 200 to 900 nm. The absorbance at 375 and 535 nm had the stronger intensity of Cu-TCPP and Cu-TCPP/Ti₃C₂, which originated from the porphyrinic structure of Cu-TCPP [31]. Besides, the obvious redshift of peaks for Cu-TCPP/Ti₃C₂ confirmed the strong interaction in the interface between Cu-TCPP and Ti₃C₂. The addition of Ti₃C₂ enhanced the absorbance of Cu-TCPP under 400–900 nm. Thus, it was promising to improve the photothermal performance under 660 + 808 light. The bandgap (E_g) was calculated by the Tauc plot in Fig. S7. The bandgap of Cu-TCPP and Cu-TCPP/Ti₃C₂ was 1.98, 1.91 eV, respectively. The reduced bandgap after the combination of Cu-TCPP and Ti₃C₂ was beneficial to the excitement of photogenerated electrons. The extinction spectra of Ti₃C₂ suspension were measured in Fig. S8. Its localized surface plasmon resonance (LSPR) absorption band of Ti₃C₂ was 760 nm [32]. Thus, Ti₃C₂ exhibited excellent photothermal performance in the near-infrared region.

The photocurrent density of Ti₃C₂, Cu-TCPP, and Cu-TCPP/Ti₃C₂ under 660, 660 + 808 nm was measured, respectively. As shown in Fig. 3b, under 660 nm irradiation, Cu-TCPP/Ti₃C₂ had the biggest photocurrent density, whereas Cu-TCPP only had a smaller value and Ti₃C₂ had hardly any value. Thus, Cu-TCPP can be stimulated by 660 nm light to produce photogenerated carriers. And the addition of Ti₃C₂ can improve the transfer of electrons. Under 660 + 808 nm irradiation, the photocurrent density of each group was higher than those under individual 660 nm. And the photocurrent density of Cu-TCPP/Ti₃C₂ significantly increased compared to those of Ti₃C₂ and Cu-TCPP under 660 + 808 nm irradiation. Thus, the addition of Ti₃C₂ promoted electron transfer, increasing the utilization of electrons. Besides, the photocurrent density of Cu-TCPP/Ti₃C₂ under different light power of 808 nm was measured. As shown in Fig. S9, the photocurrent density gradually improved with the increase of light power of 808 nm. Even if the power increased to 1.41 W cm⁻², the photocurrent density only increased to 0.56 μ A cm⁻², which increased by 2.8 times compared to the photocurrent density under individual 660 nm (0.20 μ A cm⁻²). To verify the role of heat, the photocurrent density of Cu-TCPP/Ti₃C₂ at 25 and 55 °C was measured. As shown in Fig. S10, the photocurrent density at 55 °C (1.44 μ A cm⁻²) was higher than that at 25 °C (0.56 μ A cm⁻²). The photocurrent density under 55 °C improved 7.2 times compared to the photocurrent density under individual 660 nm. Thus, heat played a vital role in the transfer of electrons. In comparison, the heat dramatically enhanced the photocurrent density, and accelerate the transfer of electrons [33]. The electrochemical impedance spectroscopy (EIS) was measured to explore the charge transfer dynamics. As shown in Fig. 3c, Cu-TCPP had the biggest semicircle, suggesting that electron transfer can suffer from stronger resistance. The smaller semicircle of Cu-TCPP/Ti₃C₂ indicated that the addition of Ti₃C₂ decreased the resistance of electron transfer.

Additionally, the photoluminescence (PL) spectra were measured to demonstrate the recombination efficiency of photogenerated electrons and holes. As shown in Fig. 3d, a stronger PL signal of Cu-TCPP can be observed, while the peak of Cu-TCPP/Ti₃C₂ drastically decreased, suggesting that photogenerated electrons and holes of Cu-TCPP/Ti₃C₂ can be efficiently separated, improving the utilization of electrons.

The production of ROS was measured under 660 + 808 nm by DCFH for Ti₃C₂, Cu-TCPP, and Cu-TCPP/Ti₃C₂. In Fig. 3e, both Ctrl and Ti₃C₂ groups only produced negligible ROS. The yield of ROS of Cu-TCPP and Cu-TCPP/Ti₃C₂ gradually increased with the extension of light time. Cu-TCPP showed few ROS under the same condition. In contrast, Cu-TCPP/Ti₃C₂ enhanced the yield of ROS. In addition, Fig. S11 compared the production of ROS for Cu-TCPP/Ti₃C₂ under 25 °C and 55 °C. Obviously, more ROS can be generated under 55 °C, demonstrating that heat improved the utilization of electrons to produce more ROS.

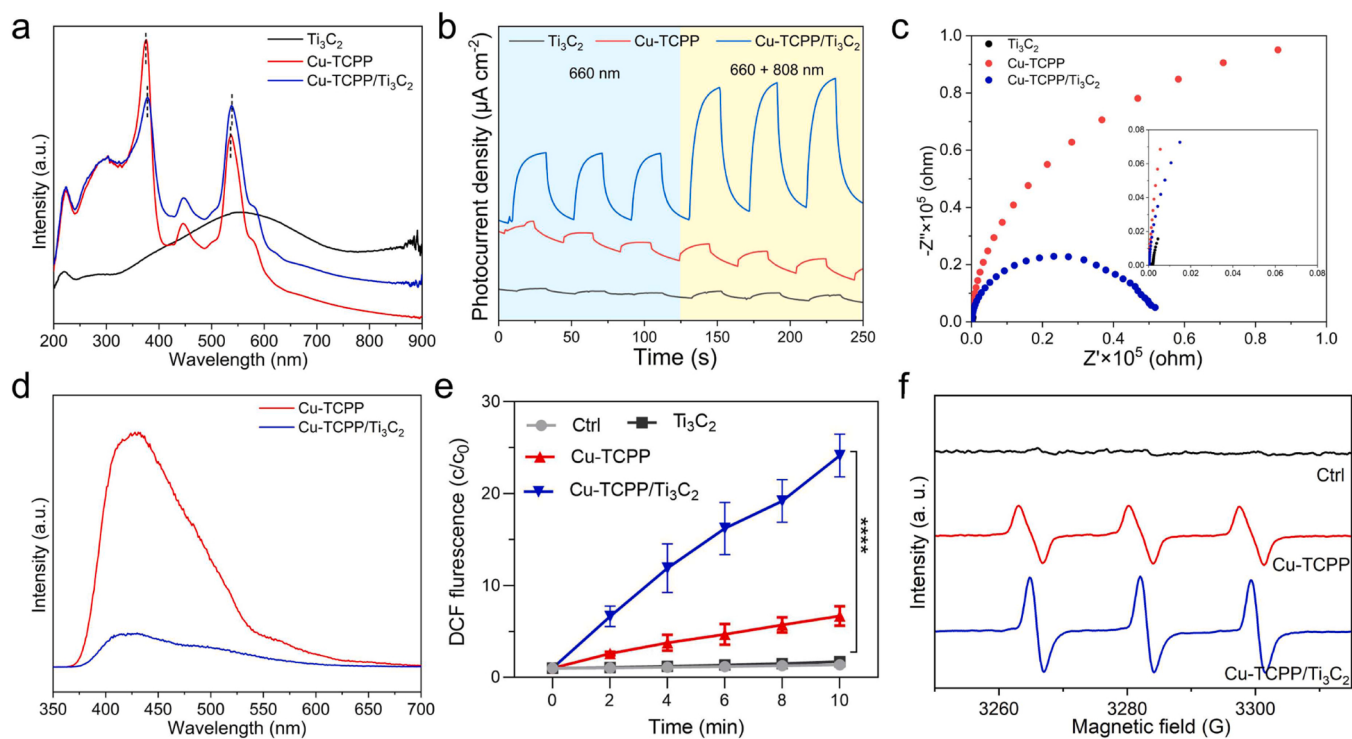


Fig. 3. Photocatalytic performance of Cu-TCPP/Ti₃C₂. (a) UV–vis absorbance spectra. (b) Photocurrent density of Ti₃C₂, Cu-TCPP, and Cu-TCPP/Ti₃C₂ under light irradiation. (c) EIS spectra without light. (d) Steady-state PL spectra of Cu-TCPP and Cu-TCPP/Ti₃C₂. (e) ROS production with DCFH fluorescence probe under 660 + 808 nm light irradiation. (f) ESR spectra of ¹O₂.

The species of ROS was measured by electron spin resonance (ESR), 1, 3-diphenylisobenzofuran (DPBF), aminophenyl fluorescein (APF), and nitro blue tetrazolium (NBT). Firstly, the singlet oxygen (¹O₂) was

measured by ESR. Compared to Ctrl, 1: 1: 1 signal in Fig. 3f can be observed for Cu-TCPP and Cu-TCPP/Ti₃C₂ under light irradiation, indicating the generation of ¹O₂. The stronger peak intensity of Cu-

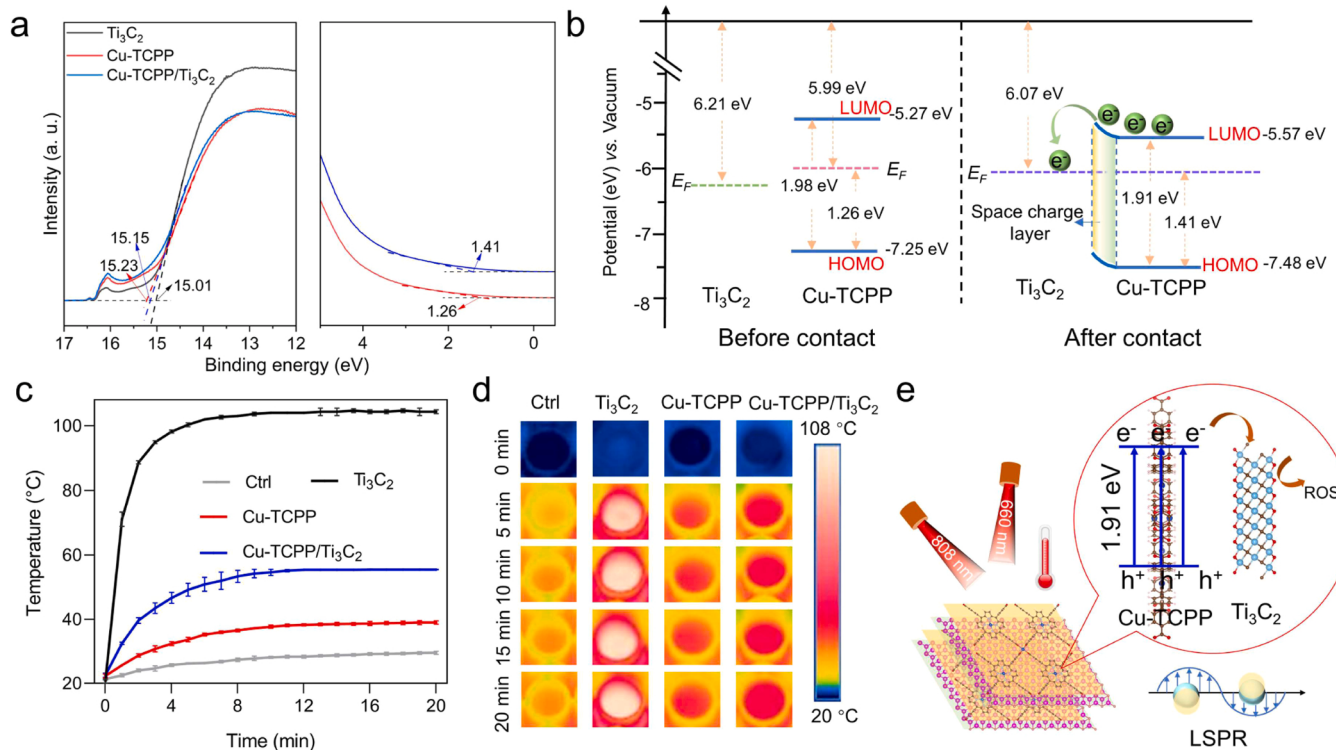


Fig. 4. Photocatalytic mechanism and photothermal performance of Cu-TCPP/Ti₃C₂. (a) UPS spectra measured by He I ($\hbar\nu = 21.22$ eV) spectra and valence band of Cu-TCPP and Cu-TCPP/Ti₃C₂. (b) Energy scheme before and after contact of Ti₃C₂ and Cu-TCPP. (c) Photothermal curves of Ti₃C₂, Cu-TCPP, and Cu-TCPP/Ti₃C₂ with 660 + 808 nm light irradiation. (d) Photothermal images. (e) Schematic illustration of the mechanism of enhanced photocatalytic and photothermal ability.

TCPP/Ti₃C₂ suggested Cu-TCPP/Ti₃C₂ can produce more ¹O₂ under light irradiation. Meanwhile, 1, 3-diphenylisobenzofuran (DPBF) also was used to measure the generation of ¹O₂. As shown in Fig. S12, the absorbance intensity of Cu-TCPP/Ti₃C₂ was far lower than that of Cu-TCPP. This result also revealed Cu-TCPP/Ti₃C₂ can produce more ¹O₂. The hydroxyl radical (·OH) and superoxide radical (·O₂[·]) were measured by APF and NBT, respectively. As shown in Fig. S13a, b, few fluorescence and no obvious absorbance can be detected for Cu-TCPP/Ti₃C₂. EPR data further demonstrated that Cu-TCPP/Ti₃C₂ can produce few ·OH cannot generate ·O₂[·]. Thus, Cu-TCPP/Ti₃C₂ mainly produced ¹O₂ under light irradiation. ¹O₂ is accepted as the main mediator of photocytotoxicity, which can cause biomembrane oxidation and degradation, further accelerating the death of bacteria [34].

The level of band energy was an important parameter to analyze the electron transfer behavior of the interface. Thus, the work function (W_F) was assessed by ultraviolet photoelectron spectroscopy (UPS) to calculate the level of band energy. As shown in Fig. 4a, the secondary electron cutoff energy (E_{cutoff}) of Ti₃C₂ and Cu-TCPP was 15.01, 15.23 eV, respectively. Thus, the W_F can be calculated to be 6.21 and 5.99 eV by subtracting the excitation energy of He I (21.22 eV). Namely, the Fermi level (E_F) of Ti₃C₂ and Cu-TCPP with respect to vacuum level was 6.21 and 5.99 eV, respectively. After the combination of Ti₃C₂ and Cu-TCPP, the E_{cutoff} was 15.15 eV, corresponding to 6.07 eV of W_F. The reduced W_F of Cu-TCPP/Ti₃C₂ compared to Cu-TCPP improve the ability of electron transition, accelerating the transfer of electrons. In addition, the highest occupied molecular orbital (HOMO) with respect to E_F of Cu-TCPP and Cu-TCPP/Ti₃C₂ was 1.26, 1.41 eV, respectively. Thus, the level of HOMO of Cu-TCPP and Cu-TCPP/Ti₃C₂ with respect to vacuum level was –7.25, –7.48 eV. According to the result of the bandgap, the level of the lowest unoccupied molecular orbital (LUMO) of Cu-TCPP and Cu-TCPP/Ti₃C₂ can be calculated to –5.27, –5.57 eV, respectively. Based on the above results, the energy level of Ti₃C₂ and Cu-TCPP was exhibited in Fig. 4b. Before contact with Ti₃C₂ and Cu-TCPP, the energy level was exhibited on the left side of this figure. The Fermi level of Cu-TCPP was higher than that of Ti₃C₂. After the combination of Ti₃C₂ and Cu-TCPP, the electrons were spontaneously transferred from Cu-TCPP to Ti₃C₂ until the equilibrium state of the Fermi level due to the difference of W_F. The accompanying band bending and the Schottky barrier can be formed. According to the above result, the energy band positions can satisfy the redox potential of O₂/¹O₂ (1.88 V vs NHE) [35]. ¹O₂ can be produced by Cu-TCPP/Ti₃C₂ under light.

The photothermal performance of Ti₃C₂, Cu-TCPP, and Cu-TCPP/Ti₃C₂ was recorded in Figs. 4c and 4d. Under 660 + 808 nm irradiation, Ctrl group only rose to 27.6 °C during 20 min. The temperature of Ti₃C₂, Cu-TCPP, and Cu-TCPP/Ti₃C₂ groups can reach 104.3, 39.0, and 55.5 °C, respectively. The corresponding figures can be exhibited in Fig. 4d.

The mechanism of enhanced photocatalytic and photothermal ability for Cu-TCPP/Ti₃C₂ was exhibited in Fig. 4e. Under light irradiation, Cu-TCPP/Ti₃C₂ can absorb more photons, which can excite Cu-TCPP to produce photogenerated carriers. The electrons can jump from HOMO to LUMO and transfer to the side of Ti₃C₂ by the tight interface. The existence of the Schottky barrier can inhibit the flow of electrons, improving the utilization of electrons. And Ti₃C₂ can rapidly capture electrons, inhibiting the recombination of electrons and holes due to its excellent conductivity. The intimate contact of Cu-TCPP and Ti₃C₂ can provide a convenient transfer channel. Besides, the addition of Ti₃C₂ enhanced the light absorption under 808 nm. The enhanced photothermal effect is attributed to the LSPRs, in which confined free electrons oscillate with the same frequency as the incident radiation. The produced hot electrons may collide with the lattice atom, resulting in enhanced temperature [36]. And the heat accelerated the transfer of electrons, producing more ROS. Thus, the structure of 2D MOF anchored Ti₃C₂ MXene nanosheet improved the photocatalysis and photothermal performance.

3.3. The photocatalytic mechanism of Cu-TCPP/Ti₃C₂

To further clarify the mechanism of the enhanced yield of ROS, density functional theory (DFT) calculations were studied in Fig. 5. As shown in Fig. 5a, the density of state (DOS) of Cu-TCPP exhibited that the LUMO was mainly derived from the C and N atoms and the HOMO was predominantly composed of Cu, N, and O atoms. Ti₃C₂ had substantial electronic states crossing the Fermi level, suggesting metallic characteristics in Fig. 5b. The electronic band structure of Cu-TCPP in Fig. S14a exhibited the direct-gap semiconductor characteristic with the bandgap of 1.11 eV. The band structure of Ti₃C₂ also demonstrated the metallic characteristic in Fig. S14b. The band structure of Cu-TCPP/Ti₃C₂ in Fig. 5c showed the hybridized level due to the addition of Ti₃C₂.

Additionally, the work function was calculated to investigate the interface of Cu-TCPP and Ti₃C₂. As shown in Fig. 5d-f, the work function of Cu-TCPP, Ti₃C₂, and Cu-TCPP/Ti₃C₂ were 4.58, 5.89, and 4.62 eV, respectively. The work function of Cu-TCPP is lower than that of Ti₃C₂. That is, the Fermi energy (E_F) of Cu-TCPP was higher than that of Ti₃C₂. After Cu-TCPP and Ti₃C₂ were contacted, the electrons on the side of Cu-TCPP can transfer to the side of Ti₃C₂ until the equilibrium due to the difference of work function. As shown in Fig. 5g-h, the differential charge density demonstrated that electrons gathered on the side of Ti₃C₂. Meantime, the line profile of plane-averaged differential charge density ($\Delta\rho$) along z direction also suggested the redistribution of interface charges and electron depletion was distributed on the side of Cu-TCPP. It can be inferred that electrons can transfer from Cu-TCPP to Ti₃C₂.

To effectively understand the photocatalysis, the adsorption of oxygen molecules (O₂) on the surface of Cu-TCPP, Ti₃C₂, and Cu-TCPP/Ti₃C₂ was evaluated. The crystalline structure in Fig. S15 showed the active sites of Cu₂O₈ sites and CuN₄ sites. In Fig. 5i, the position of adsorbed O₂ of Cu-TCPP was presented. The adsorption energies were –0.46 eV of Cu₂O₈ sites and –0.29 eV of CuN₄ sites. The adsorption energy of Ti₃C₂ was –0.15 eV in Fig. S16. –0.42 eV of Cu₂O₈ sites and –0.27 eV of CuN₄ sites located in the interface of Ti₃C₂ and Cu-TCPP for Cu-TCPP/Ti₃C₂ can be obtained in Fig. 5j. Thus, the addition of Ti₃C₂ hardly change the ability of adsorption energies of Cu-TCPP, suggesting that O₂ still can be adsorbed on the surface of Cu-TCPP/Ti₃C₂.

Based on the DFT result, the mechanism of improved ROS was exhibited in Fig. 6. The interface of Cu-TCPP and Ti₃C₂ formed Schottky barrier and space charge layer due to the different work function. When Cu-TCPP/Ti₃C₂ was irradiated by 660 + 808 nm, Cu-TCPP was excited to produce photogenerated electrons, which were rapidly transferred to Ti₃C₂. The intimate close provided a rapid electron transfer channel across the interface. Consequently, the separation efficiency of photo-generated electron-hole pairs was significantly enhanced by rapid transfer and inhibition of electron backflow. The enhanced photothermal performance also accelerated the transfer of electrons. Thus, Cu-TCPP/Ti₃C₂ can produce more ROS under 660 + 808 nm. In this process, O₂ firstly was absorbed on the surface of Cu-TCPP/Ti₃C₂. Molecular oxygen in its ground state exists in the triplet state (³Σ_g[·]), namely ³O₂. Under light irradiation, Cu-TCPP triplet transferred energy and exhibited charge transfer to ground-state ³O₂ to produce ¹O₂ [37,38].

3.4. The antibacterial performance of Cu-TCPP/Ti₃C₂ in vitro

Under light irradiation, Cu-TCPP/Ti₃C₂ possessed excellent photothermal and photocatalytic performance. Thus, it was promising to achieve antibacterial performance. *Staphylococcus aureus* (*S. aureus*) was used to measure the antibacterial performance. The antibacterial performance of Cu-TCPP/Ti₃C₂-X was measured under 660 + 808 nm light. As shown in Fig. S17, the bacterial counts gradually reduced with the increase of Ti₃C₂ content by the spread plate result. The corresponding antibacterial rate was 78.65 ± 3.96%, 84.25 ± 0.78%, 99.93 ± 0.03%, 99.98 ± 0.03% for Cu-TCPP/Ti₃C₂-1, Cu-TCPP/Ti₃C₂-3, Cu-TCPP/Ti₃C₂-5, and Cu-TCPP/Ti₃C₂-7, respectively. Cu-TCPP/Ti₃C₂-7 had

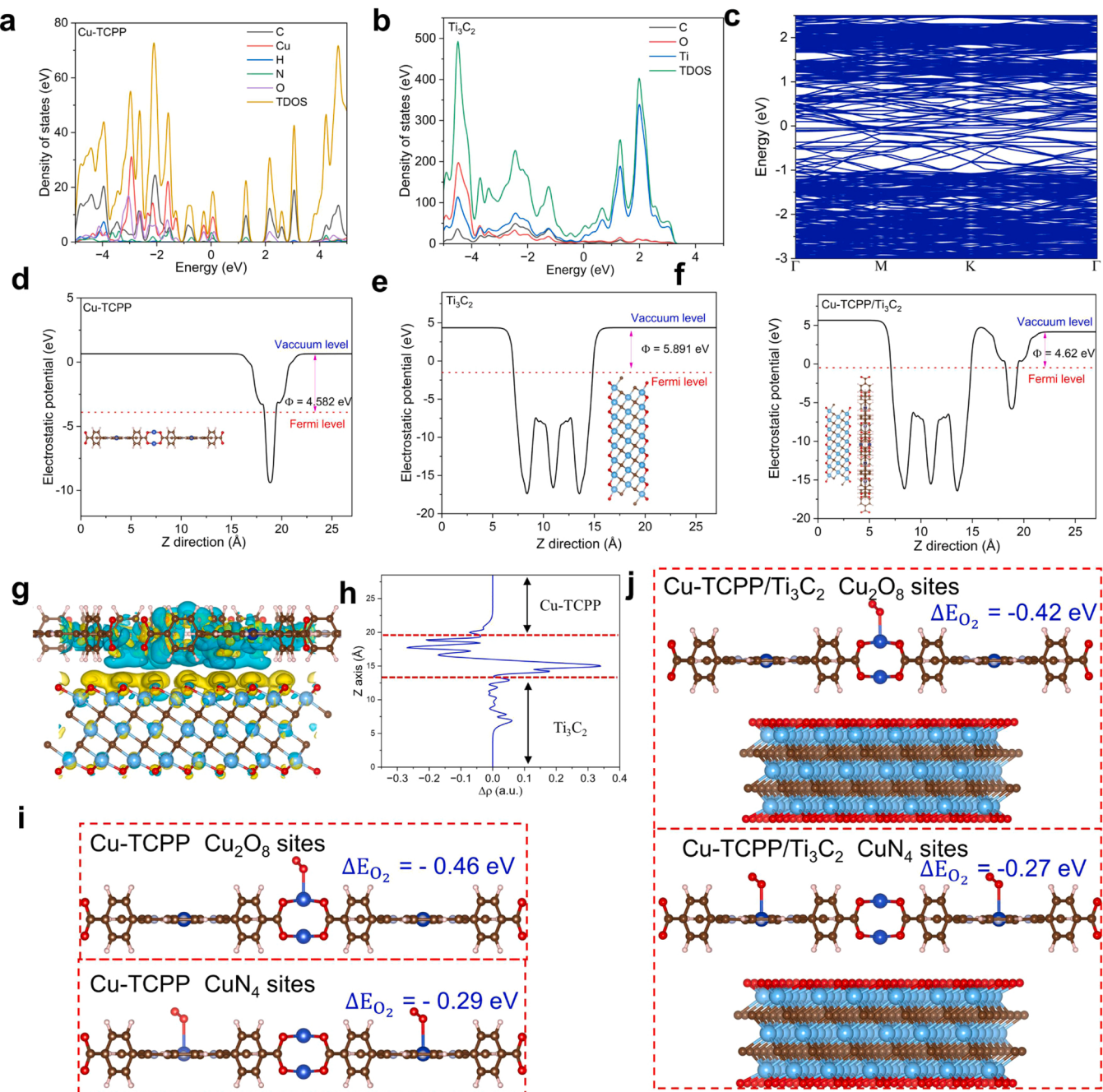


Fig. 5. The mechanism of enhanced ROS of Cu-TCPP/Ti₃C₂. (a) DOS of Cu-TCPP. (b) DOS of Ti₃C₂. (c) Electronic band structure of Cu-TCPP/Ti₃C₂. (d-f) The work function of Cu-TCPP (d), Ti₃C₂ (e), and Cu-TCPP/Ti₃C₂ (f). (g) The differential charge density of Cu-TCPP/Ti₃C₂. Yellow and green isosurfaces are represented as electron accumulation and depletion, respectively. (h) Profile of the plane-averaged differential charge density along z-axis. (i-j) The adsorption energy after O₂ absorption on Cu-TCPP (i) and Cu-TCPP/Ti₃C₂ (j).

excellent antibacterial performance due to hyperthermia. Too much temperature can injure the skin, which was not beneficial to the practical application. The result suggested the combined effect of ROS and the suitable photothermal performance can show good antibacterial effect to use antibacterial application.

The antibacterial performance of Cu-TCPP, Ti₃C₂, and Cu-TCPP/Ti₃C₂ was measured. As shown in Fig. 7a, all the plates had lots of bacterial counts in the absence of light for 20 min, indicating a negligible antibacterial effect. The bacterial counts of Cu-TCPP were similar to that of Ctrl group. Only a few bacteria can be observed for Cu-TCPP/Ti₃C₂ under light, suggesting excellent antibacterial performance. No bacteria can be found in Ti₃C₂ group due to the excellent photothermal

performance under 660 + 808 nm light. Fig. 7b showed the bacterial counts for each group without or with light. No obvious antibacterial efficiency can be found for each group in the dark. Cu-TCPP/Ti₃C₂ can kill $99.74 \pm 0.12\%$ of *S. aureus* under light irradiation. Moreover, Cu-TCPP/Ti₃C₂ showed cyclic antibacterial effect against $99.9987 \pm 0.0012\%$ after two cycles of antimicrobial tests. The corresponding spread plate images were exhibited in Fig. S18.

Additionally, the antibacterial performance of Cu-TCPP/Ti₃C₂ under 660 nm or 808 nm alone was assessed. As shown in Fig. S19, the antibacterial effect under 660 nm or 808 nm alone was $25.66 \pm 7.19\%$, $62.54 \pm 8.69\%$, demonstrating individual 660 nm or 808 nm light cannot excite Cu-TCPP/Ti₃C₂ to kill bacteria. To explore the influence of

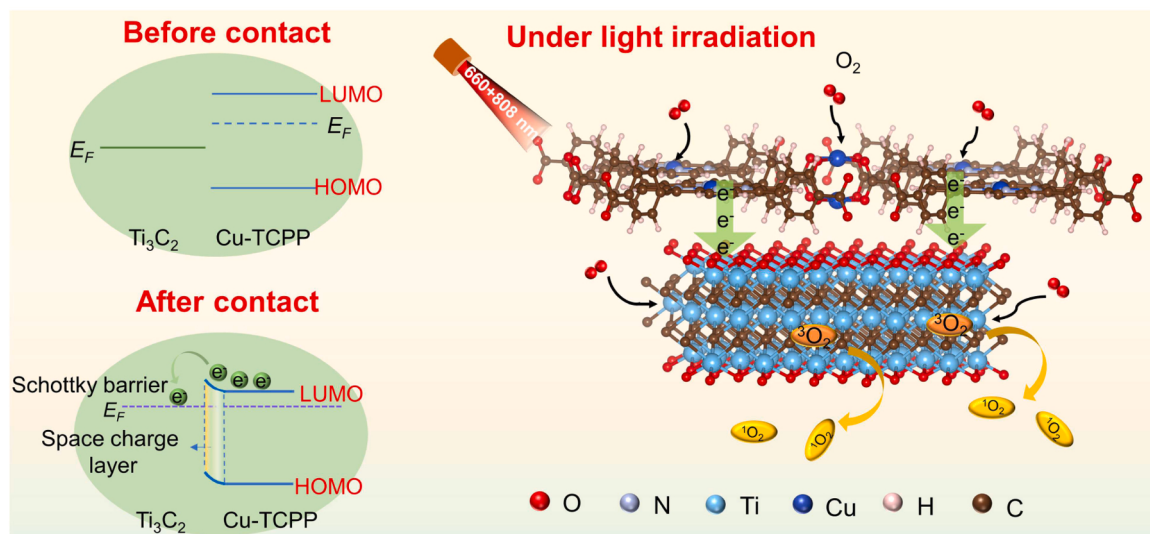


Fig. 6. The mechanism scheme of enhanced ROS of Cu-TCPP/Ti₃C₂.

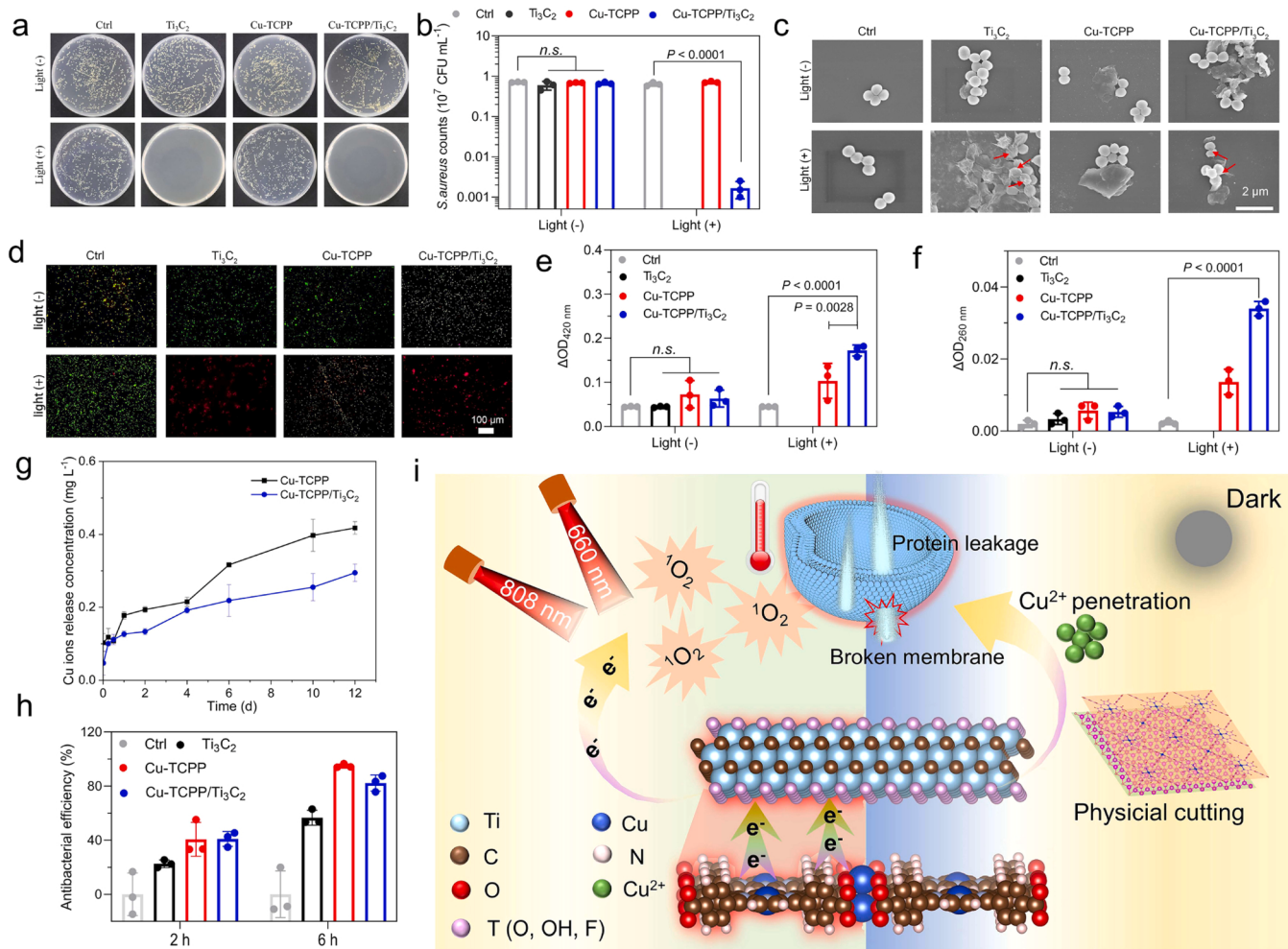


Fig. 7. The antibacterial performance of Cu-TCPP/Ti₃C₂. (a) The spread plate result of Ti₃C₂, Cu-TCPP, and Cu-TCPP/Ti₃C₂ without or with 660 + 808 nm light irradiation. (b) The bacterial counts of Ti₃C₂, Cu-TCPP, and Cu-TCPP/Ti₃C₂. (c) The bacterial SEM images of Ti₃C₂, Cu-TCPP, and Cu-TCPP/Ti₃C₂. (d) Live/dead staining fluorescence images. (e) The ONPG hydrolysis assay. (f) The absorbance at 260 nm in *S. aureus*. (g) The release of Cu ions from Cu-TCPP and Cu-TCPP/Ti₃C₂ in 100 mL of deionized water at 37 °C. (h) The antibacterial efficiency of Ti₃C₂, Cu-TCPP, and Cu-TCPP/Ti₃C₂ in the dark for 2 and 6 h. (i) The antibacterial mechanism of Cu-TCPP/Ti₃C₂.

heat and ROS, the antibacterial performance was measured in **Fig. S20**. The antibacterial efficiency of heat or ROS was $54.06 \pm 2.19\%$, $30.66 \pm 3.16\%$, respectively. Heat or ROS was far lower than that under light irradiation, and the sum of antibacterial rate was also lower than that under light irradiation (i. e., $54.06\% + 30.66\% < 99.74\%$). This result suggested heat or ROS alone cannot reach effective antibacterial ability and the synergy role of ROS and heat can reach excellent antibacterial activity. The temperature of Cu-TCPP/Ti₃C₂ can reach 20.2 °C for 20 min in ice-water bath under 660 + 808 nm (**Fig. S21**).

SEM images of bacteria were exhibited in **Fig. 7c**. The intact and smooth spheres can be observed in the dark for every group. Under light, the bacteria membrane had serve shrinking for Ti₃C₂ and Cu-TCPP/Ti₃C₂ groups, marked as the red arrows. The live/dead staining fluorescence images were exhibited in **Fig. 7d**. The fluorescence of each group in the dark for 20 min was green, suggesting the live bacteria. Almost all of the fluorescence for Ti₃C₂ and Cu-TCPP/Ti₃C₂ groups was red under light irradiation, revealing the dead bacteria.

The bacterial membrane permeability was investigated by ONPG (2-Nitrophenyl β-D-galactopyranoside) in **Fig. 7e**. In the dark, the value of each group had no significant difference for 20 min, indicating the intact membrane structure. Under light irradiation, the value at 420 nm for Cu-TCPP/Ti₃C₂ significantly increased, suggesting the broken cell membrane. Additionally, the ONPG of Cu-TCPP/Ti₃C₂ also was assessed under temperature controlling (20 °C) or light irradiation in **Fig. S22**. The value at 420 nm apparently reduced compared to that under 660 + 880 nm. Thus, heat can accelerate the destruction of bacterial membranes, leading to the death of bacteria. When the bacterial membrane is disturbed, the release of the cytoplasmic constituents can be monitored. The absorbance at 260 nm was measured to detect cytoplasmic leakage. In **Fig. 7f**, no obvious difference between every group with dark due to the integrated bacterial membrane. Under light, the enhanced OD_{260 nm} value for Cu-TCPP/Ti₃C₂ illustrated the rupture of the bacterial membrane and the leakage of the content of cells. According to the above result, the synergy of ROS and heat can destroy bacterial membrane, resulting in the leakage of cytoplasmic constituents and the death of bacteria. Under light irradiation, the localized temperature can destruct bacterial cells by thermal denaturation of protein and thermomechanical damage [39]. And ROS can attract bacteria to break its defense function, destroying metabolic function [40].

The Cu ions release of Cu-TCPP and Cu-TCPP/Ti₃C₂ during 12 d was measured by ICP. In **Fig. 7g**, only a small amount of Cu ions can be released in the dark for 20 min. The release of Cu ions for Cu-TCPP and Cu-TCPP/Ti₃C₂ gradually increased. The released amount of Cu ions for Cu-TCPP/Ti₃C₂ was fewer than that of Cu-TCPP. Thus, the combination of Cu-TCPP and Ti₃C₂ can decrease the release of Cu ions. Additionally, the released amount of Cu ions of Cu-TCPP/Ti₃C₂ also was assessed under light for 20 min in **Fig. S23**. The release of Cu ions under light was higher than that in the dark, revealing that light irradiation can accelerate the release of Cu ions. The amount of Cu ions still had no obvious influence on bacteria for 20 min due to the slow release and short time [41].

The antibacterial performance of materials in the dark for 2 and 6 h was measured. In **Fig. 7h** and **Fig. S24**, after 2 h, Cu-TCPP, Ti₃C₂, and Cu-TCPP/Ti₃C₂ had different antibacterial effects. The antibacterial rates were $40.66 \pm 12.58\%$, $22.58 \pm 2.84\%$, and $40.98 \pm 5.45\%$, respectively. After 6 h, their antibacterial effects were $94.87 \pm 1.46\%$, $56.60 \pm 5.54\%$, and $82.21 \pm 5.95\%$, respectively. Thus, the antibacterial rate gradually increased with the increase in incubation time. The antibacterial performance of Ti₃C₂ mainly originated from the role of physical cutting in the dark [42]. The excellent antibacterial effect of Cu-TCPP and Cu-TCPP/Ti₃C₂ was resulting from the release of Cu ions and physical damage. During incubation, continuous shaking can drive the edge of nanosheets to cut or insert the cell membranes and vigorously extract large amounts of phospholipids from the membranes, resulting in the death of bacteria [43].

The antibacterial mechanism of Cu-TCPP/Ti₃C₂ without or with light

was shown in **Fig. 7i**. Under 660 + 808 nm light irradiation, Cu-TCPP/Ti₃C₂ can absorb more photons, which can excite more carriers. The photogenerated electrons can jump from HOMO to LUMO and quickly transfer from Cu-TCPP to the side of Ti₃C₂ due to the close contact. Besides, electrons were difficult to backflow due to the formation of Schottky barrier between the interface of Cu-TCPP and Ti₃C₂. Thus, more electrons can be utilized to produce ROS. These ROS can attack bacterial cell envelope to damage the cell membrane integrity [44], decreasing the viability of bacteria. Moreover, LSPR effect of Ti₃C₂ excited by light can generate high-energy hot electrons, which can cause lattice vibrations and local heating of metal nanocrystals [45]. Thus, the addition of Ti₃C₂ improved the photothermal effect. The photothermal effect can improve the transfer of electrons and the utilization of electrons, producing more ROS. The synergistic effect of ROS and heat destroyed metabolic function, accelerating the death of bacteria [46]. Thus, bacteria were rapidly killed with the synergy of ROS and heat for 20 min under 660 + 808 nm light. In the dark, Cu-TCPP/Ti₃C₂ can slowly release Cu ions. These Cu ions can combine with cell membrane to kill bacteria. And the physical damage of 2D materials also played a part role. Thus, Cu-TCPP/Ti₃C₂ can kill bacteria under light irradiation for 20 min or in the dark for long time.

3.5. Biocompatibility *in vivo*

The cell viability of materials was evaluated by the 3-[4, 5-dimethylthiazol-2-yl]-2, 5-diphenyltetrazolium bromide (MTT). In **Fig. S25a**, the cell viability of Cu-TCPP/Ti₃C₂ was 83.61% compared to that of Ctrl group after 3 d, illustrating the weaker cell cytotoxicity due to the release of Cu ions. Additionally, the fluorescence images in **Fig. S25b** showed that the cells for each group had complete cytoplasmic spreading and filopodia extension, suggesting that these materials had no obvious cell cytotoxicity.

3.6. Wound healing *in vivo*

The wound model of rats was constructed to evaluate the antibacterial effect *in vivo*. In **Fig. 8a**, the graph of wounds revealed the gradual healing during 12 d. After 7 d, the wound area had an obvious decrease for Cu-TCPP/Ti₃C₂ + light (+) group, while significant suppuration can be observed around wounds for TCPP/Ti₃C₂ + light (-) and Ctrl groups. After 12 d, the wound of Cu-TCPP/Ti₃C₂ + light (+) had nearly healed, while the wounds of Cu-TCPP/Ti₃C₂ + light (-) and Ctrl groups still had large wounds. Thus, Cu-TCPP/Ti₃C₂ + light (+) can kill bacteria, achieving a good therapeutic effect.

The blood routine at 2 and 12 d was used to assess the bacterial infection in **Fig. 8b**. The higher value of white blood cells (WBC), lymphocytes (Lymph), monocytes (Mon), and granulocyte (Gran) of Ctrl and Cu-TCPP/Ti₃C₂ + light (-) groups suggested the inflammatory response *in vivo*. These values of Cu-TCPP/Ti₃C₂ + light (+) groups were within the normal range. Besides, the red blood cell (RBC), hemoglobin (HGB), and platelet (PLT) of each group were maintained within the normal range, suggesting that Cu-TCPP/Ti₃C₂ had no obvious cell cytotoxicity *in vivo*.

Fig. 8c recorded the variety of temperatures of wounds under light. During 20 min, the temperature rose from 36.9 °C to 52.5 °C. The bacterial counts of wounds treated after 2 d were quantified by spread plate method. As shown in **Fig. 8d**, Ctrl and Cu-TCPP/Ti₃C₂ + light (-) groups had lots of bacteria. Cu-TCPP/Ti₃C₂ + light (+) group exhibited excellent antibacterial performance ($96.56 \pm 0.35\%$).

Hematoxylin and eosin (H&E) staining of wound tissue was shown in **Fig. 8e**. The number of inflammatory cells in Ctrl and Cu-TCPP/Ti₃C₂ + light (-) groups was far higher than that of TCPP/Ti₃C₂ + light (+) group after 2 d. Even 12 d, Ctrl and Cu-TCPP/Ti₃C₂ + light (-) groups still had few neutrophils around the wounds. Besides, Giemsa staining of wound tissue was measured in **Fig. 8f**. After 2 d, a large number of bacteria appeared in the Ctrl and Cu-TCPP/Ti₃C₂ + light (-) groups,

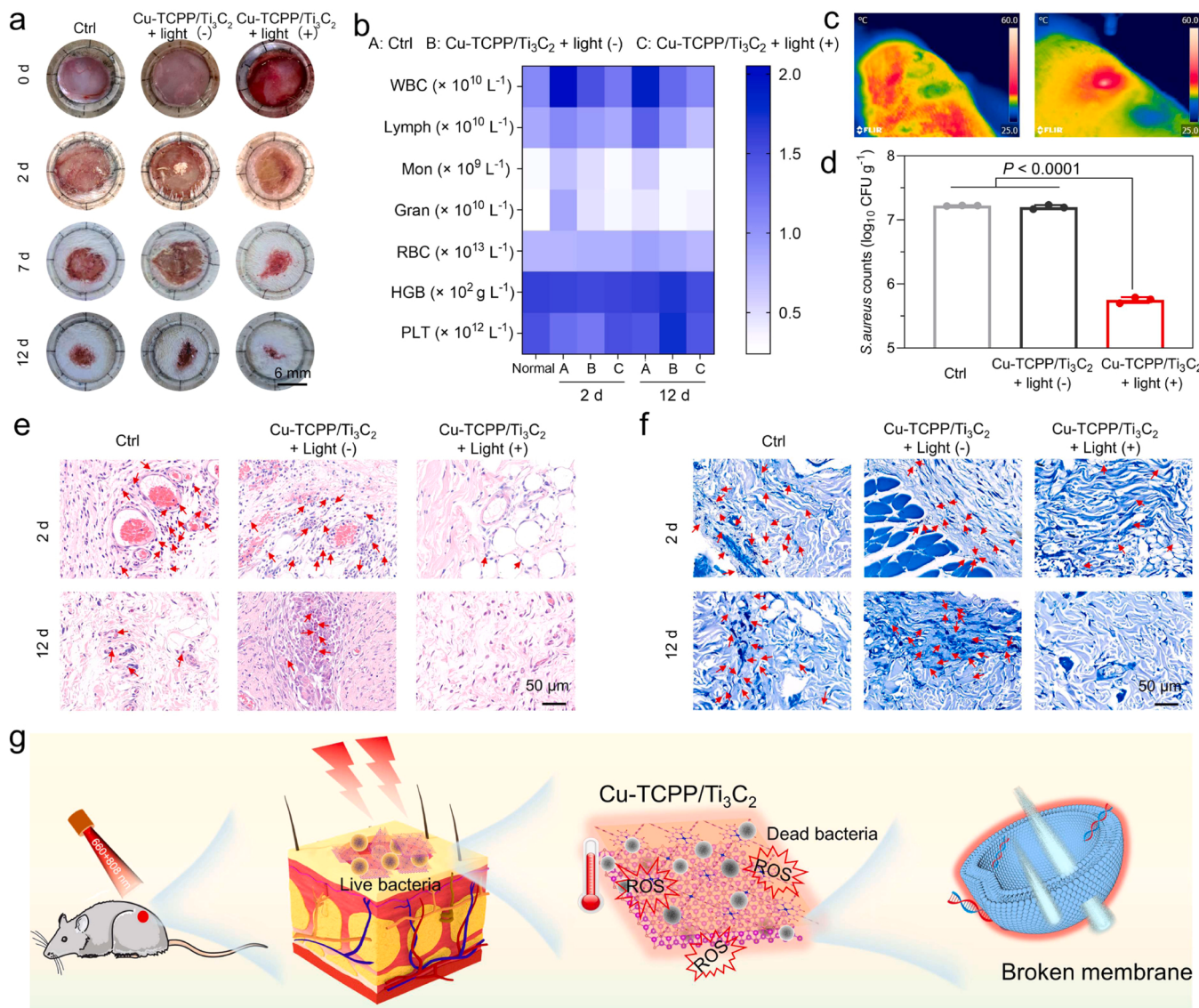


Fig. 8. The antibacterial assay in vivo. (a) The representative wound images of rats collected on 0, 2, 7, 12 d for Ctrl, Cu-TCPP/Ti₃C₂ + light (-), and Cu-TCPP/Ti₃C₂ + Light (+) groups. (b) Blood routine of each group after 2 d and 12 d. (c) The photothermal images of Cu-TCPP/Ti₃C₂ + Light (+) groups under light irradiation. (d) The bacterial counts on wound for Ctrl, Cu-TCPP/Ti₃C₂ + Light (-), and Cu-TCPP/Ti₃C₂ + Light (+) groups. (e) H&E staining of wound tissue for each group on 2 and 12 d. (f) Giemsa staining of wound tissue for each group on 2 and 12 d. (g) The schematic diagram antibacterial performance.

while only a few bacteria can be found in Cu-TCPP/Ti₃C₂ + light (+) group. After 12 d, Cu-TCPP/Ti₃C₂ + light (+) group was almost hard to find bacteria. This result suggested that Cu-TCPP/Ti₃C₂ can achieve rapid sterilization under light irradiation in vivo.

Additionally, Masson staining on 2 and 12 d was exhibited in Fig. S26. More collagen deposition was presented for Cu-TCPP/Ti₃C₂ under light, indicating the best tissue regeneration ability. However, the loose and disordered collagen can be observed for Ctrl and Cu-TCPP/Ti₃C₂ + light (-) groups due to tissue inflammation around wounds.

The toxicity of Cu-TCPP/Ti₃C₂ in vivo was evaluated by H&E staining of the heart, liver, spleen, lung, and kidney. These groups had no obvious organ damage (Fig. S27), indicating the good biosecurity of Cu-TCPP/Ti₃C₂.

All results indicated that the antibacterial effects of Cu-TCPP/Ti₃C₂ under 660 + 808 nm light irradiation depended on the synergistic actions of heat and ROS (Fig. 8g). These ROS and heat can rapidly kill bacteria by disrupting the membrane structure, decreasing the risk of wound infection. In consequence, the tissue around the wound rapidly formed collagen fibers, thus promoting wound healing.

4. Conclusions

We have successfully synthesized Ti₃C₂ MXene-anchored 2D MOF heterojunction to reach excellent antibacterial performance under 660 + 808 nm light irradiation through an interface engineering strategy. 2D MOF/Ti₃C₂ heterojunction with a close structure can provide a convenient path of electron transfer, effectively improving the separation of electrons and holes. The formation of Schottky junction in the interface between MOF and Ti₃C₂ inhibited the flowback of electrons, enhancing the utilization of carriers. The improved photothermal performance of MOF/Ti₃C₂ improved photocatalytic performance. The wound model demonstrated MOF/Ti₃C₂ can rapidly kill bacteria in vivo, facilitating the healing of the wound. This work can provide more thought for the design of photo-responsive materials for the therapy of bacteria-infected wounds or photocatalytic applications.

CRediT authorship contribution statement

Jianfang Li: Conceptualization, Data curation, Investigation, Formal

analysis, Writing – original draft. **Chaofeng Wang**: Data curation, Methodology. **Shuilin Wu**: Conceptualization, Formal analysis, Writing – review & editing. **Yufeng zheng**: Writing - review & editing. **Zhenduo Cui**: Writing – review & editing. **Hui Jiang**: Investigation, Methodology. **Zhaoyang Li**: Investigation, Methodology. **Shengli Zhu**: Data curation, Writing – review & editing. **Liheng Feng**: Formal analysis, Writing – original draft. **Xiangmei Liu**: Methodology, Writing – review & editing.

Declaration of Competing Interest

The authors declare that they have no known competing financial interests or personal relationships that could have appeared to influence the work reported in this paper.

Data Availability

Data will be made available on request.

Acknowledgment

This work is jointly supported by the China National Funds for Distinguished Young Scientists (No. 51925104), and the National Natural Science Foundation of China (No 52173251), NSFC-Guangdong Province Joint Program (Key program no. U21A2084), the Central Guidance on Local Science and Technology Development Fund of Hebei Province (6Z1303G).

Appendix A. Supporting information

Supplementary data associated with this article can be found in the online version at [doi:10.1016/j.apcatb.2023.123163](https://doi.org/10.1016/j.apcatb.2023.123163).

References

- U. Theuretzbacher, S. Gottwalt, P. Beyer, M. Butler, L. Czaplewski, C. Lienhardt, L. Moja, M. Paul, S. Paulin, J.H. Rex, L.L. Silver, M. Spigelman, G.E. Thwaites, J.-P. Paccaud, S. Harbarth, Analysis of the clinical antibacterial and antituberculosis pipeline, *Lancet Infect. Dis.* 19 (2019) 40–50.
- Y. Li, X. Liu, Z. Cui, Y. Zheng, H. Jiang, Y. Zhang, Z. Li, S. Zhu, S. Wu, Treating multi-drug-resistant bacterial infections by functionalized nano-bismuth sulfide through the synergy of immunotherapy and bacteria-sensitive phototherapy, *ACS Nano* 16 (2022) 14860–14873.
- H. Zhu, B. Li, X. Liu, Y. Qiao, Y. Lv, Y. Zheng, S. Zhu, Z. Li, Z. Cui, J. Shen, S. Wu, Interfacial Mo, W-conjugated polarization, and oxygen vacancies of MoO_2/WO_3 in enhanced microwave therapy for MRSA-induced osteomyelitis, *ACS Nano* 16 (2022) 21098–21110.
- C.J.L. Murray, K.S. Ikuta, F. Sharara, L. Swetschinski, G. Robles Aguilera, A. Gray, C. Han, C. Bisignano, P. Rao, E. Wool, S.C. Johnson, A.J. Browne, M.G. Chipeta, F. Fell, S. Hackett, G. Haines-Woodhouse, B.H. Kashef Hamadani, E.A.P. Kumaran, B. McManigal, R. Agarwal, S. Akech, S. Albertson, J. Amusai, J. Andrews, A. Aravkin, E. Ashley, F. Bailey, S. Baker, B. Basnyat, A. Bekker, R. Bender, A. Bethou, J. Bielicki, S. Boonkasidecha, J. Bokosia, C. Carvalheiro, C. Castañeda-Orjuela, V. Chansamouth, S. Chaurasia, S. Chirchirù, F. Chowdhury, A.J. Cook, B. Cooper, T.R. Cressey, E. Criollo-Mora, M. Cunningham, S. Darboe, N.P.J. Day, M. De Luca, K. Dokova, A. Dramowski, S.J. Dunachie, T. Eckmanns, D. Eibach, A. Emami, N. Feasey, N. Fisher-Pearson, K. Forrest, D. Garrett, P. Gastmeier, A. Z. Giref, R.C. Greer, V. Gupta, S. Haller, A. Haselbeck, S.I. Hay, M. Holm, S. Hopkins, K.C. Iregbu, J. Jacobs, D. Jarovsky, F. Javanmardi, M. Khorana, N. Kissoon, E. Kobeissi, T. Kostyanev, F. Krapp, R. Krumkamp, A. Kumar, H.H. Kyu, C. Lim, D. Limmathurotsakul, M.J. Loftus, M. Lunn, J. Ma, N. Mturi, T. Munera-Huertas, P. Musicha, M.M. Mussi-Pinhata, T. Nakamura, R. Nanavati, S. Ngangia, P. Newton, C. Ngoun, A. Novotney, D. Nwakanma, C.W. Obiero, A. Olivas-Martinez, P. Olliaro, E. Ooko, E. Ortiz-Brizuela, A.Y. Peleg, C. Perrone, N. Plakkal, A. Ponce-de-Leon, M. Raad, T. Ramdin, A. Riddell, T. Roberts, J.V. Robotham, A. Roca, K.E. Rudd, N. Russell, J. Schnall, J.A.G. Scott, M. Shivamallappa, J. Sifuentes-Osorio, N. Steenkeste, A.J. Stewardson, T. Stoeva, N. Tasak, A. Thaiprakong, G. Thwaites, C. Turner, P. Turner, H.R. van Doorn, S. Velaphi, A. Vongpradith, H. Vu, T. Walsh, S. Waner, T. Wangrangsimakul, T. Wozniak, P. Zheng, B. Sartorius, A.D. Lopez, A. Stergachis, C. Moore, C. Dolecek, M. Naghavi, Global burden of bacterial antimicrobial resistance in 2019: a systematic analysis, *Lancet* 399 (2022) 629–655.
- J. Li, Z. Li, X. Liu, C. Li, Y. Zheng, K.W.K. Yeung, Z. Cui, Y. Liang, S. Zhu, W. Hu, Y. Qi, T. Zhang, X. Wang, S. Wu, Interfacial engineering of $\text{Bi}_2\text{S}_3/\text{Ti}_3\text{C}_2\text{Tx}$ MXene based on work function for rapid photo-excited bacteria-killing, *Nat. Commun.* 12 (2021) 1224.
- H. Lin, Y. Wang, S. Gao, Y. Chen, J. Shi, Theranostic 2D tantalum carbide (MXene), *Adv. Mater.* 30 (2018) 1703284.
- J. Su, G.D. Li, X.H. Li, J.S. Chen, 2D/2D heterojunctions for catalysis, *Adv. Sci.* 6 (2019) 1801702.
- W. Song, J. Chen, Z. Li, X. Fang, Self-powered MXene/GaN van der waals heterojunction ultraviolet photodiodes with superhigh efficiency and stable current outputs, *Adv. Mater.* 33 (2021) 2101059.
- R. Yang, Y. Fan, Y. Zhang, L. Mei, R. Zhu, J. Qin, J. Hu, Z. Chen, Y. Hau Ng, D. Voiry, S. Li, Q. Lu, Q. Wang, J.C. Yu, Q. Zeng, 2D transition metal dichalcogenides for photocatalysis, *Angew. Chem. Int. Ed.* 62 (2023) e202218016.
- H. Wang, X. Zhang, Y. Xie, Photocatalysis in two-dimensional black phosphorus: the roles of many-body effects, *ACS Nano* 12 (2018) 9648–9653.
- D. Han, X. Liu, S. Wu, Metal organic framework-based antibacterial agents and their underlying mechanisms, *Chem. Soc. Rev.* 51 (2022) 7138–7169.
- Y. Wang, L. Feng, J. Pang, J. Li, N. Huang, G.S. Day, L. Cheng, H.F. Drake, Y. Wang, C. Lollar, J. Qin, Z. Gu, T. Lu, S. Yuan, H.C. Zhou, Photosensitizer-anchored 2D MOF nanosheets as highly stable and accessible catalysts toward artemisinin production, *Adv. Sci.* 6 (2019) 1802059.
- D. Yang, S. Zuo, H. Yang, Y. Zhou, Q. Lu, X. Wang, Tailoring layer number of 2D porphyrin-based MOFs towards photocoupled electroreduction of CO_2 , *Adv. Mater.* 34 (2022) 2107293.
- L. Wang, P. Jin, S. Duan, H. She, J. Huang, Q. Wang, In-situ incorporation of Copper(II) porphyrin functionalized zirconium MOF and TiO_2 for efficient photocatalytic CO_2 reduction, *Sci. Bull.* 64 (2019) 926–933.
- K.S. Novoselov, A. Mishchenko, A. Carvalho, A.H. Castro, Neto, 2D materials and van der Waals heterostructures, *Science* 353 (2016) 9439.
- W. Wang, G. Li, T. An, D.K.L. Chan, J.C. Yu, P.K. Wong, Photocatalytic hydrogen evolution and bacterial inactivation utilizing sonochemical-synthesized g- C_3N_4 /red phosphorus hybrid nanosheets as a wide-spectral-responsive photocatalyst: the role of type I band alignment, *Appl. Catal. B* 238 (2018) 126–135.
- J. Wu, Y. Zhang, P. Lu, G. Fang, X. Li, W.W. Yu, Z. Zhang, B. Dong, Engineering 2D multi-hetero-interface in the well-designed nanosheet composite photocatalyst with broad electron-transfer channels for highly-efficient solar-to-fuels conversion, *Appl. Catal. B* 286 (2021), 119944.
- J. Li, L. Ma, Z. Li, X. Liu, Y. Zheng, Y. Liang, C. Liang, Z. Cui, S. Zhu, S. Wu, Oxygen vacancies-rich heterojunction of $\text{Ti}_3\text{C}_2/\text{BiOB}$ for photo-excited antibacterial textiles, *Small* 18 (2022) 2104448.
- A. Agresti, A. Pazniak, S. Pescetelli, A. Di Vito, D. Rossi, A. Pecchia, M. Auf der Maur, A. Liedl, R. Larciprete, D.V. Kuznetsov, D. Saranin, A. Di Carlo, Titanium-carbide MXenes for work function and interface engineering in perovskite solar cells, *Nat. Mater.* 18 (2019) 1228–1234.
- Q. Lian, L. Hu, D. Ma, Y. Jiao, D. Xia, Y. Huang, Z. Tang, W. Qu, H. Zhao, C. He, D. D. Gang, Interstitial atomic Bi Charge-alternating processor boosts twofold molecular oxygen activation enabling rapid catalytic oxidation reactions at room temperature, *Adv. Func. Mater* 32 (2022) 2205054.
- W. Liu, P. Wang, Y. Ao, J. Chen, X. Gao, B. Jia, T. Ma, Directing charge transfer in a chemical-bonded $\text{BaTiO}_3/\text{ReS}_2$ Schottky heterojunction for piezoelectric enhanced photocatalysis, *Adv. Mater.* 34 (2022) 2202508.
- M. Alhabeb, K. Maleski, B. Anasori, P. Lelyukh, L. Clark, S. Sin, Y. Gogotsi, Guidelines for synthesis and processing of two-dimensional titanium carbide ($\text{Ti}_3\text{C}_2\text{Tx}$ MXene), *Chem. Mater.* 29 (2017) 7633–7644.
- M. Ahmad, X. Quan, S. Chen, H. Yu, Tuning Lewis acidity of MIL-88B-Fe with mixed-valence coordinatively unsaturated iron centers on ultrathin Ti_3C_2 nanosheets for efficient photo-Fenton reaction, *Appl. Catal. B* 264 (2020), 118534.
- M.S. Yao, J.W. Xiu, Q.Q. Huang, W.H. Li, W.W. Wu, A.Q. Wu, L.A. Cao, W.H. Deng, G.E. Wang, G. Xu, Van der waals, heterostructured MOF-on-MOF thin films: cascading functionality to realize advanced chemiresistive sensing, *Angew. Chem. Int. Ed.* 58 (2019) 14915–14919.
- Y. Zhao, J. Wang, R. Pei, Micron-sized, Ultra Met. Framew. Sheet, *J. Am. Chem. Soc.* 142 (2020) 10331–10336.
- Y. Li, Z. Gao, F. Chen, C. You, H. Wu, K. Sun, P. An, K. Cheng, C. Sun, X. Zhu, B. Sun, Decoration of cisplatin on 2D metal-organic frameworks for enhanced anticancer effects through highly increased reactive oxygen species generation, *ACS Appl. Mater. Interfaces* 10 (2018) 30930–30935.
- Q. Xue, H. Zhang, M. Zhu, Z. Pei, H. Li, Z. Wang, Y. Huang, Y. Huang, Q. Deng, J. Zhou, S. Du, Q. Huang, C. Zhi, Photoluminescent Ti_3C_2 MXene quantum dots for multicolor cellular imaging, *Adv. Mater.* 29 (2017) 1604847.
- S. Zhao, S. Li, Z. Zhao, Y. Su, Y. Long, Z. Zheng, D. Cui, Y. Liu, C. Wang, X. Zhang, Z. Zhang, Microwave-assisted hydrothermal assembly of 2D copper-porphyrin metal-organic frameworks for the removal of dyes and antibiotics from water, *Environ. Sci. Pollut. Res. Int.* 27 (2020) 39186–39197.
- Y. Xu, H. Gong, H. Ren, X. Fan, P. Li, T. Zhang, K. Chang, T. Wang, J. He, Highly efficient Cu-porphyrin-based metal-organic framework nanosheet as cathode for high-rate $\text{Li}-\text{CO}_2$ battery, *Small* 18 (2022) 2203917.
- F. He, B. Zhu, B. Cheng, J. Yu, W. Ho, W. Macyk, 2D/2D/0D $\text{TiO}_2/\text{C}_3\text{N}_4/\text{Ti}_3\text{C}_2$ MXene composite S-scheme photocatalyst with enhanced CO_2 reduction activity, *Appl. Catal. B* 272 (2020), 119006.
- F. Yang, W. Hu, C. Yang, M. Patrick, A.L. Cooksey, J. Zhang, J.A. Aguiar, C. Fang, Y. Zhou, Y.S. Meng, J. Huang, J. Gu, Tuning internal strain in metal-organic frameworks via vapor phase infiltration for CO_2 reduction, *Angew. Chem. Int. Ed. Engl.* 59 (2020) 4572–4580.
- C. Wang, X.-G. Nie, Y. Shi, Y. Zhou, J.-J. Xu, X.-H. Xia, H.-Y. Chen, Direct plasmon-accelerated electrochemical reaction on gold nanoparticles, *ACS Nano* 11 (2017) 5897–5905.
- J. Tian, L. Chen, R. Qiao, K. Xiong, W. Zhang, Y. Mao, H. Li, J. Li, Photothermal-assist enhanced high-performance self-powered photodetector with bioinspired

temperature-autoregulation by passive radiative balance, *Nano Energy* 79 (2021), 105435.

[34] R. Bakalova, H. Ohba, Z. Zhelev, M. Ishikawa, Y. Baba, Quantum dots as photosensitizers? *Nat. Biotechnol.* 22 (2004) 1360–1361.

[35] Q. Lian, W. Liu, D. Ma, Z. Liang, Z. Tang, J. Cao, C. He, D. Xia, Precisely orientating atomic array in one-dimension tellurium microneedles enhances intrinsic piezoelectricity for an efficient piezo-catalytic sterilization, *ACS Nano* 17 (2023) 8755–8766.

[36] X. Wu, J. Wang, Z. Wang, F. Sun, Y. Liu, K. Wu, X. Meng, J. Qiu, Boosting the electrocatalysis of MXenes by plasmon-induced thermalization and hot-electron injection, *Angew. Chem. Int. Ed.* 60 (2021) 9416–9420.

[37] Y. Nosaka, A.Y. Nosaka, Generation and detection of reactive oxygen species in photocatalysis, *Chem. Rev.* 117 (2017) 11302–11336.

[38] J. Li, S. Song, J. Meng, L. Tan, X. Liu, Y. Zheng, Z. Li, K.W.K. Yeung, Z. Cui, Y. Liang, S. Zhu, X. Zhang, S. Wu, 2D MOF periodontitis photodynamic ion therapy, *J. Am. Chem. Soc.* 143 (2021) 15427–15439.

[39] D. Xia, Q. Chen, Y. Jiao, Q. Lian, M. Sun, C. He, J. Shang, T. Wang, A modified flower pollen-based photothermocatalytic process for enhanced solar water disinfection: photoelectric effect and bactericidal mechanisms, *Water Res* 217 (2022), 118423.

[40] Z. Tang, R. Yin, W. Qu, H. Liu, H. Luo, D. Xia, Y. Huang, L. Shu, C. He, Flower pollen-based photosensitization process for enhanced solar disinfection of drinking water: reactor design and inactivation mechanisms, *ACS EST Eng.* 2 (2022) 629–641.

[41] C. Ning, X. Wang, L. Li, Y. Zhu, M. Li, P. Yu, L. Zhou, Z. Zhou, J. Chen, G. Tan, Y. Zhang, Y. Wang, C. Mao, Concentration ranges of antibacterial cations for showing the highest antibacterial efficacy but the least cytotoxicity against mammalian cells: implications for a new antibacterial mechanism, *Chem. Res. Toxicol.* 28 (2015) 1815–1822.

[42] K. Rasool, M. Helal, A. Ali, C.E. Ren, Y. Gogotsi, K.A. Mahmoud, Antibacterial activity of $Ti_3C_2T_x$ MXene, *ACS Nano* 10 (2016) 3674–3684.

[43] Y. Tu, M. Lv, P. Xiu, T. Huynh, M. Zhang, M. Castelli, Z. Liu, Q. Huang, C. Fan, H. Fang, R. Zhou, Destructive extraction of phospholipids from *Escherichia coli* membranes by graphene nanosheets, *Nat. Nanotechnol.* 8 (2013) 594–601.

[44] W. Wang, H. Xie, G. Li, J. Li, P.K. Wong, T. An, Visible light-induced marine bacterial inactivation in seawater by an in situ photo-fenton system without additional oxidants: implications for ballast water sterilization, *ACS ES&T, Water* 1 (2021) 1483–1494.

[45] G. Yu, J. Qian, P. Zhang, B. Zhang, W. Zhang, W. Yan, G. Liu, Collective excitation of plasmon-coupled Au-nanochain boosts photocatalytic hydrogen evolution of semiconductor, *Nat. Commun.* 10 (2019) 4912.

[46] Q. Lian, Z. Liang, X. Guan, Z. Tang, R. Zhang, B. Yang, Y. Wu, H. Zhao, C. He, D. Xia, High-coordinated BiV/BiIV regulates photocatalytic selective activation of structural oxygen and self-generated H_2O_2 dominating an efficient synergistic sterilization, *Appl. Catal. B* 331 (2023), 122724.